Application of Multiscale Cohesive Zone Model to Simulate Fracture in Polycrystalline Solids

Jing Qian

Department of Civil and Environmental Engineering,
University of California,
Berkeley, CA 94720

Shaofan Li[1]

e-mail: shaofan@berkeley.edu
Department of Civil and Environmental Engineering,
University of California,
Berkeley, CA 94720;
School of Civil Engineering and Mechanics,
Huazhong University of Science and Technology,
Wuhan 430074, P.R. China

In this work, we apply the multiscale cohesive method (Zeng and Li, 2010, "A Multiscale Cohesive Zone Model and Simulations of Fracture," Comput. Methods Appl. Mech. Eng., 199, pp. 547–556) to simulate fracture and crack propagations in polycrystalline solids. The multiscale cohesive method uses fundamental principles of colloidal physics and micromechanics homogenization techniques to link the atomistic binding potential with the mesoscale material properties of the cohesive zone and hence, the method can provide an effective means to describe heterogeneous material properties at a small scale by taking into account the effect of inhomogeneities such as grain boundaries, bimaterial interfaces, slip lines, and inclusions. In particular, the depletion potential of the cohesive interface is made consistent with the atomistic potential inside the bulk material and it provides microstructure-based interface potentials in both normal and tangential directions with respect to finite element boundary separations. Voronoi tessellations have been utilized to generate different randomly shaped microstructure in studying the effect of polycrystalline grain morphology. Numerical simulations on crack propagation for various cohesive strengths are presented and it demonstrates the ability to capture the transition from the intergranular fracture to the transgranular fracture. A convergence test is conducted to study the possible size-effect of the method. Finally, a high-speed impact example is reported. The example demonstrates the advantages of multiscale cohesive method in simulating the spall fracture under high-speed impact loads.
[DOI: 10.1115/1.4002647]

1 Introduction

Due to the exponential growth in microelectronic devices and extensive application of ceramics and ceramic composites, the reliability of polycrystalline materials has become a major concern because most of ceramics and metals are in polycrystalline form in which each grain may have a different crystallographic orientation, shape, and size. The discrete nature of crystallographic, which refers to the distribution of the grain orientations [1] and the slip along certain lattice directions on preferred crystallographic planes, entails an anisotropic plastic response [2–5]. Many theories have been developed at various size scales, from homogenized solids to grain level and even atomistic modeling. There are mainly two classes of models that have been developed in past decade [6]. The first class of models belongs to the continuum damage model [7–10], which is based on homogenization of material properties. Although it is well known that microstructure characteristics such as grain shape, spatial arrangement of grains and local crystallographic orientation can obviously influence the materials response, most existing macroscopic nonlocal constitutive models lack a rigorous description of the role of lattice orientations of constituent grains and the effects of crystal morphology on failure process [11,12].

An alternative approach is to combine the so-called cohesive finite element method and polycrystalline constitutive modeling. In the past decade, the cohesive finite element method has gained much popularity [6,13–17]. Such methods employ a so-called cohesive zone that is embedded along the edges of finite elements, which may mimic surface decohesion by a prescribed empirical surface of traction-displacement relation. By doing so, stress singularity can be avoided. Moreover, the crack initiation or propagation does not rely on any artificial criterion but a natural outcome of simulations.

In most of the cohesive interface element methods, the traction-displacement relations are such that with increasing interfacial separation, the traction across the interface reaches a maximum then decreases and eventually vanishes, permitting a complete decohesion. In principle, an ideal paradigm of cohesive zone model should be the one that is built on *an exact mesoscale cohesive potential* in the sense that this exact mesoscale cohesive potential is derived from the atomistic potential based on first-principle calculation if it is all possible. So far, most of these applications are macroscale material failure analysis and the traction cohesive laws adopted are empirical traction-displacement relation. However, the empirical cohesive law may reach to its limit of submicron scale because small scale plasticity is highly size-dependent.

On the other hand, the multiscale approach has been viewed as the most promising candidate that may ultimately replace the empirical cohesive potential approach. In a recent work, Zeng and Li [18] have proposed and implemented a multiscale cohesive zone model. They have successfully built a multiscale cohesive zone model to relate the mesoscale interface properties to the atomistic potential, which naturally takes into account material microstructures such as interface lattice orientation and rotation. In this method, there are two coarse graining models: one for the bulk medium and the other for the material interfaces or defects. By constructing a finite-width cohesive zone and extending the Cauchy–Born rule to coarse scale deformation field, the multiscale cohesive zone model can simulate the overall behaviors of a nonuniform deformation caused by defects. With the aid of the
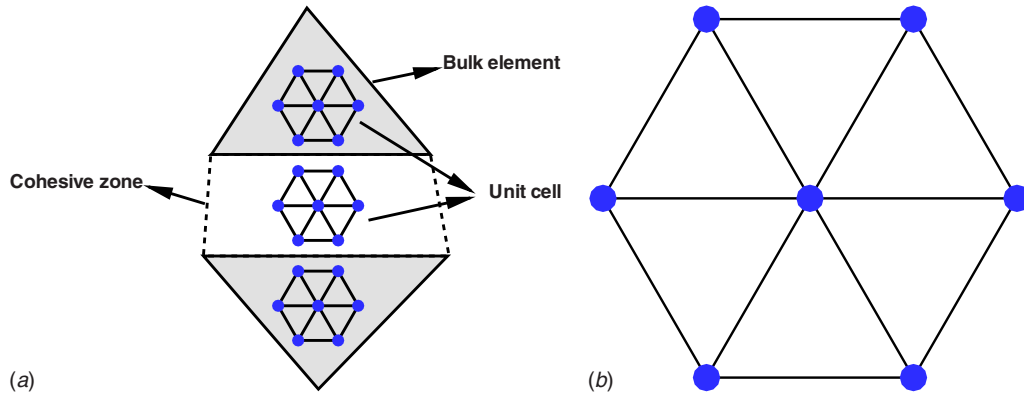
Fig. 1 Multiscale cohesive zone model: (a) triangular bulk element and cohesive zone and (b) hexagonal lattice used in this paper

multiscale cohesive zone method, it is much easier and more efficient to study polycrystalline materials in grain level with full consideration of microstructure characteristics.

2 A Multiscale Cohesive Zone Method

In the multiscale cohesive zone method, the global nonuniform deformation field may be represented by a macroscale piece-wise uniform deformation field that consists of the bulk element of uniformed deformation, which are connected together by finite-width cohesive zones with highly nonuniform deformations. Meanwhile, the Cauchy–Born rule was proposed to model the effective constitutive properties of the cohesive zone, as well as in bulk elements, as shown in Fig. 1(a). The beauty of such coarse-grain procedure is that the effective deformation field inside the cohesive zone can be uniquely determined by the bulk finite element nodal displacements and there is no finite element interpolation inside the cohesive zone. The coarse-grain model for the cohesive zone is properly connected with the kinematics of bulk elements. Another advantage of the multiscale cohesive zone approach is that it eliminates the discontinuous jump operator in description of the displacement field that has been employed in the conventional cohesive finite element method.

First, the cohesive zone region is assumed to be a quasi-crystalline layer with finite volume or finite thickness R_0 although there is no definite lattice structure with atomistic resolution. Indeed, the thickness R_0 can be thought as a physical parameter that is related to the characteristic length scale of specific defects in consideration. Usually, $S_0 \times 10^{-3} \leq R_0 \leq S_0 \times 10^{-1}$ and S_0 is the characteristic length of adjacent bulk elements. By assuming that the cohesive zone is a relatively "soft" interface zone, a so-called *depletion potential* was derived in the interface zone for a highly inhomogeneous deformation field inside the cohesive zone. The atomistic potential of the cohesive zone can be obtained by integrating the bulk potential over the rigid bulk medium half space with several assumptions, which the cohesive zone is a compliance interface, and it is much weaker than the adjacent bulk elements and the intermolecular interaction inside the cohesive zone is a type of the Van der Waals interaction between noncovalent bonds or quasi-covalent bonds. For instance, if the Lennard-Jones potential is chosen as the bulk potential

$$\phi_{\text{bulk}} = 4\epsilon\left(\left(\frac{\sigma}{r}\right)^{12} - \left(\frac{\sigma}{r}\right)^{6}\right) \tag{1}$$

the depletion potential of coarse graining interface can be obtained by analytical integration [19],

$$\phi_{\text{depl}}(r) = \int_{\text{half space}} \beta\phi_{\text{bulk}}(r - r')dV' = \frac{\pi\epsilon}{\sqrt{2}}\left(\frac{1}{45}\left(\frac{r_0}{r}\right)^9 - \frac{1}{3}\left(\frac{r_0}{r}\right)^3\right) \tag{2}$$

where ϵ is the depth of the potential well, σ is the finite distance at which the bulk atomistic potential is zero, $r_0 = \sigma 2^{1/6}$ is the equilibrium bond distance in the bulk material, and β is the atomic density. Therefore, the interface depletion potential has close form expressions.

2.1 Effective Deformation Gradient in Cohesive Zone. To quantitatively deal with the nonuniform deformation inside the finite-width cohesive zone, the nonuniform deformation is assumed to be multiscale in character, i.e., the displacement field inside the cohesive zone may be written as

$$\mathbf{u} = \bar{\mathbf{u}} + \mathbf{u}' \tag{3}$$

where $\bar{\mathbf{u}}$ is the coarse scale displacement field whereas $\mathbf{u}'$ is the fine scale displacement fluctuation field. With homogenization technique, the general deformation field can be represented as

$$\mathbf{x} = \bar{\mathbf{F}}\mathbf{X} + \mathbf{u}' \tag{4}$$

where $\bar{\mathbf{F}}$ may be viewed as the coarse scale deformation gradient. By using the idea of the Hill–Mandel homogenization [20], it can be proved that the average deformation gradient $\langle\mathbf{F}\rangle_{\Omega_0}$ in a cohesive zone is exactly same as $\bar{\mathbf{F}}$, i.e.,

$$\langle\mathbf{F}\rangle_{\Omega_0} = \bar{\mathbf{F}} \tag{5}$$

In particular, if the coarse scale deformation field inside the cohesive zone is compatible with the uniform deformation field inside the bulk elements, the coarse scale deformation field can then be represented by an affine function of coordinates. Hence,

$$\mathbf{F}^c \doteq \langle\mathbf{F}\rangle_{\Omega_0} = \bar{\mathbf{F}} := \left.\frac{\partial\bar{\mathbf{x}}}{\partial\mathbf{X}}\right|_{\mathbf{X}\in\Omega} \tag{6}$$

where the computation of effective deformation gradient $\mathbf{F}^c$ inside the cohesive zone can be given as (see Fig. 2)

$$\begin{bmatrix} \mathbf{F}^c_{11} \\ \mathbf{F}^c_{12} \\ \mathbf{F}^c_{21} \\ \mathbf{F}^c_{22} \end{bmatrix} = \frac{1}{(ad - cb)}\begin{bmatrix} d & 0 & -b & 0 \\ -c & 0 & a & 0 \\ 0 & d & 0 & -b \\ 0 & -c & 0 & a \end{bmatrix}\begin{bmatrix} x^+_{\ell+1} - x^-_{\ell} \\ y^+_{\ell+1} - y^-_{\ell} \\ x^+_{\ell} - x^-_{\ell+1} \\ y^+_{\ell} - x^-_{\ell+1} \end{bmatrix} \tag{7}$$
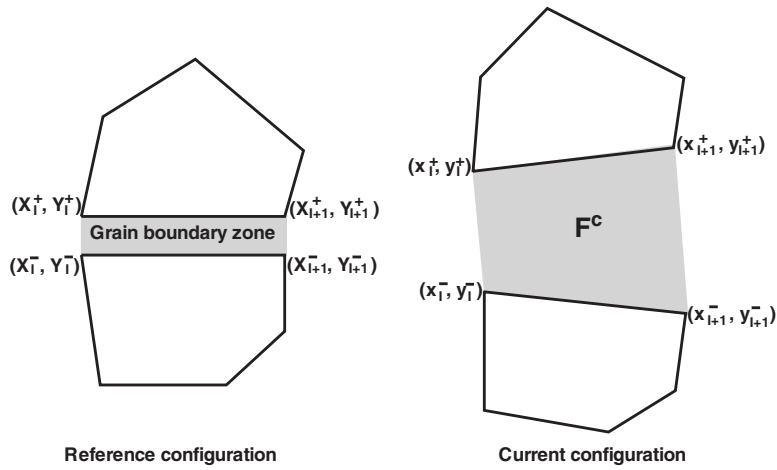
where

Fig. 2 Effected $\mathbf{F}^c$ in deformed cohesive zone

$$a = X_{\ell+1}^+ - X_\ell^-, \quad b = Y_{\ell+1}^+ - Y_\ell^-, \quad c = X_\ell^+ - X_{\ell+1}^-, \quad d = Y_\ell^+ - Y_{\ell+1}^- \tag{8}$$

2.2 Cauchy–Born Rule in Effective Field. To reduce the computational cost and complexity, the potential energy for a crystalline solid is calculated through the employed lattice model. Taking the hexagonal unit, for example, see Fig. 1(b) and bond vector $\mathbf{R}_i$ is the distance vector between the center atom and one of the atoms i located at a vertex of the unit cell. When bulk element deformation is considered as uniform, the deformed bond length is a function of deformation gradient $\mathbf{F}_e$ of the element, i.e., $r_i = |\mathbf{r}_i| = |\mathbf{F}_e \cdot \mathbf{R}_i| = r_i(\mathbf{F}_e)$. Hence, the strain energy density inside each bulk element is the function of the deformation gradient as

$$W_e = \frac{1}{\Omega_0^b} \sum_{i=1}^{n_b} \phi(r_i(\mathbf{F}_e)) = W_e(\mathbf{F}_e) \tag{9}$$

where superscript b indicates bulk element, Ω_0^b is the volume of the unit cell in the referential configuration, $\phi(r_i)$ is the atomistic potential, and r_i, $i = 1, 2, \cdots, n_b$ are the current bond lengths in a unit cell. Consequently, the constitutive relations for the bulk medium can be established. For instance, the second Piola–Kirchhoff stress can be written in the following form:

$$\mathbf{P} = \frac{1}{\Omega_0^b} \sum_{i=1}^{n_b} \frac{\partial \phi}{\partial r_i} \frac{\mathbf{r}_i \otimes \mathbf{R}_i}{r_i} \tag{10}$$

Although it can be argued to directly apply the Cauchy–Born rule in the cohesive zone because of the highly nonuniform deformation inside it, the average deformation gradient provides a means to apply the Cauchy–Born rule to the mean field of interfacial cohesive zone for simplification. It should be noticed that the use of average deformation gradient in the cohesive zone is a comprised but simplified way. For a more accurate calculation of nonuniform deformation, high order elements such as six-node or nine-node triangle elements can be employed. Similar to bulk element, the average of the deformed lattice bond vector in each cohesive zone may be calculated as follows:

$$\bar{\mathbf{r}}_i = \mathbf{F}^c \cdot \mathbf{R}_i, \quad i = 1, 2, \ldots, n_c \tag{11}$$

Subsequently, the effective first Piola–Kirchhoff stress tensor in each cohesive zone can be calculated as

$$\bar{\mathbf{P}} = \frac{\partial W}{\partial \mathbf{F}^c} = \frac{1}{\Omega_0^c} \sum_{i=1}^{n_c} \frac{\partial \phi_{\text{depl}}}{\partial \bar{r}_i} \frac{\bar{\mathbf{r}}_i \otimes \mathbf{R}_i}{\bar{r}_i} \tag{12}$$
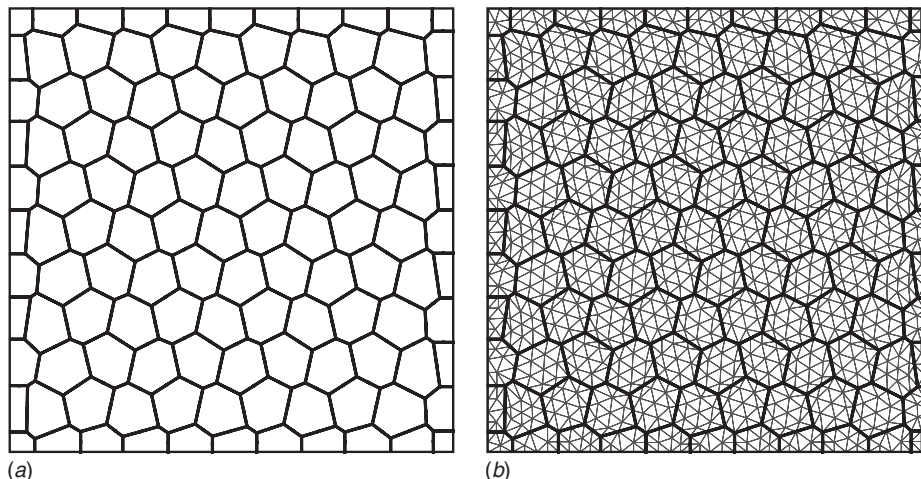

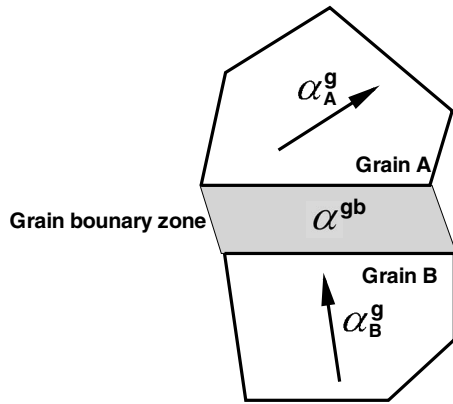**Fig. 3 Mesh generation: (a) Voronoi cell and (b) triangular bulk elements over grains**

Fig. 4 Orientation of grains and grain boundary.

3 Polycrystalline Microstructure

Voronoi tessellations have been widely utilized to generate different randomly shaped microstructures in studying the effect of polycrystalline grain morphology [6,21–24]. In this paper, the test samples are generated by the Voronoi diagram too as shown in Fig. 3(*a*). Therefore, each Voronoi cell represents a grain. Consequently, all edges of cells are considered as the grain boundaries. Then, triangular elements or bulk elements are generated over all grains. It can be seen from Fig. 3(*b*) that the meshes are conforming between grains. For the implementation of the cohesive zone method, cohesive zones are constructed on all interfaces among bulk elements.

Meanwhile, to characterize the varying grain morphology, each grain is assigned an individual set of material properties such as lattice orientation and parameters of potential. In those models used in this paper, each grain is randomly assigned a lattice orientation α^g. That means all the bulk elements in one grain have the same lattice orientation and so do the cohesive zones among them. Here, the superscript g indices granular region whereas the superscript gb denotes the zones on grain boundaries. Simultaneously, the lattice orientation of grain boundary zones α^{gb} may be assigned according to various principles and assumptions. For simplicity and demonstration purposes, the lattice orientation of the grain boundary zone as shown in Fig. 4 is taken as the average of orientations from the two adjacent grains, i.e., $\alpha^{gb} = (1/2)(\alpha_A + \alpha_B)$.

The other factor affected by granular structure is the depletion potentials of cohesive zones. Since it is not necessary that the interface zone on the grain boundary is always softer than cohe-

sive zones in grain, two hypotheses will be considered in simulations. First, both types of the cohesive zones have the same potential well depth $\epsilon^g_{\text{depl}} = \epsilon^{gb}_{\text{depl}}$. Second, the cohesive strength inside grains are stronger than that of the grain boundary, e.g., $\epsilon^g_{\text{depl}} > \epsilon^{gb}_{\text{depl}}$.

4 FEM Implementations

The Galerkin weak formulation of the multiscale cohesive zone model may be expressed as follows:

$$\sum_{e=1}^{n^b_{\text{elem}}} \left\{ \int_{B_0^e} \rho_0 \ddot{\varphi}^h \cdot \delta\varphi^h dV + \int_{B_0^e} \mathbf{P}(\varphi) : \delta\mathbf{F}^h dV \right\} + \sum_{i=1}^{n^c_{\text{elem}}} \int_{B_c^i} \mathbf{P} : \delta\mathbf{F}^c dV$$

$$= \sum_{e=1}^{n^b_{\text{elem}}} \left\{ \int_{B_0^e} \mathbf{B} \cdot \delta\varphi dV + \int_{\partial_t B_0^e} \mathbf{T}^c \cdot \delta\varphi^h dS \right\}$$

$$+ \sum_{i=1}^{n^c_{\text{elem}}} \int_{\partial_t B_c^i} \mathbf{T}^{\text{cohe}} \cdot \delta\overline{\varphi} dS \qquad (13)$$

where $\mathbf{B}$ is the body force, B_0^e is the eth element domain, $\partial_t B_0^e$ is the traction boundary of the element, and S_c^e is the cohesive boundary of the element.

Integration by parts with divergence theorem yields

$$\int_{B_c^i} \mathbf{P} : \delta\mathbf{F}^c dV = \int_{\partial B_c^i / \partial_t B_c^i} \mathbf{T}^c \cdot \delta\varphi dS + \int_{\partial_t B_c^i} \mathbf{T}^{\text{cohe}} \cdot \delta\varphi dS \quad (14)$$

for each cohesive element. Considering the fact that the boundary of the cohesive element is also the part of the boundary of the bulk element with the opposite out-normal and the fact that

$$\Gamma_t = \bigcup_{e=1}^{n^b_{\text{elem}}} \partial_t B_0^e \cup \bigcup_{i=1}^{n^c_{\text{elem}}} \partial_t B_c^i$$

the final Galerkin weak formulation of the multiscale cohesive zone model becomes

$$\sum_{e=1}^{n^b_{\text{elem}}} \left\{ \int_{B_0^e} \rho_0 \ddot{\varphi}^h \cdot \delta\varphi^h dV + \int_{B_0^e} \mathbf{P}(\varphi) : \delta\mathbf{F}^h dV - \int_{S_c^e} \mathbf{T}^{\text{cohe}} \cdot \delta\varphi^h dS \right\}$$

$$= \sum_{e=1}^{n^b_{\text{elem}}} \left\{ \int_{B_0^e} \mathbf{B} \cdot \delta\varphi dV \right\} + \int_{\Gamma_t} \mathbf{T}^{\text{cohe}} \cdot \delta\varphi dS \qquad (15)$$
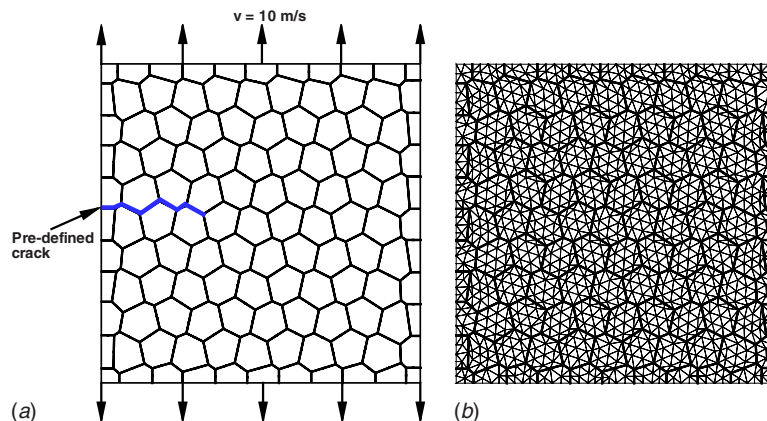
where $S_c^e := \partial B_0^e / \partial_t B_0^e$

Fig. 5 Example of unilateral tension: (*a*) sketch of unilateral tension model and (*b*) mesh of the plate
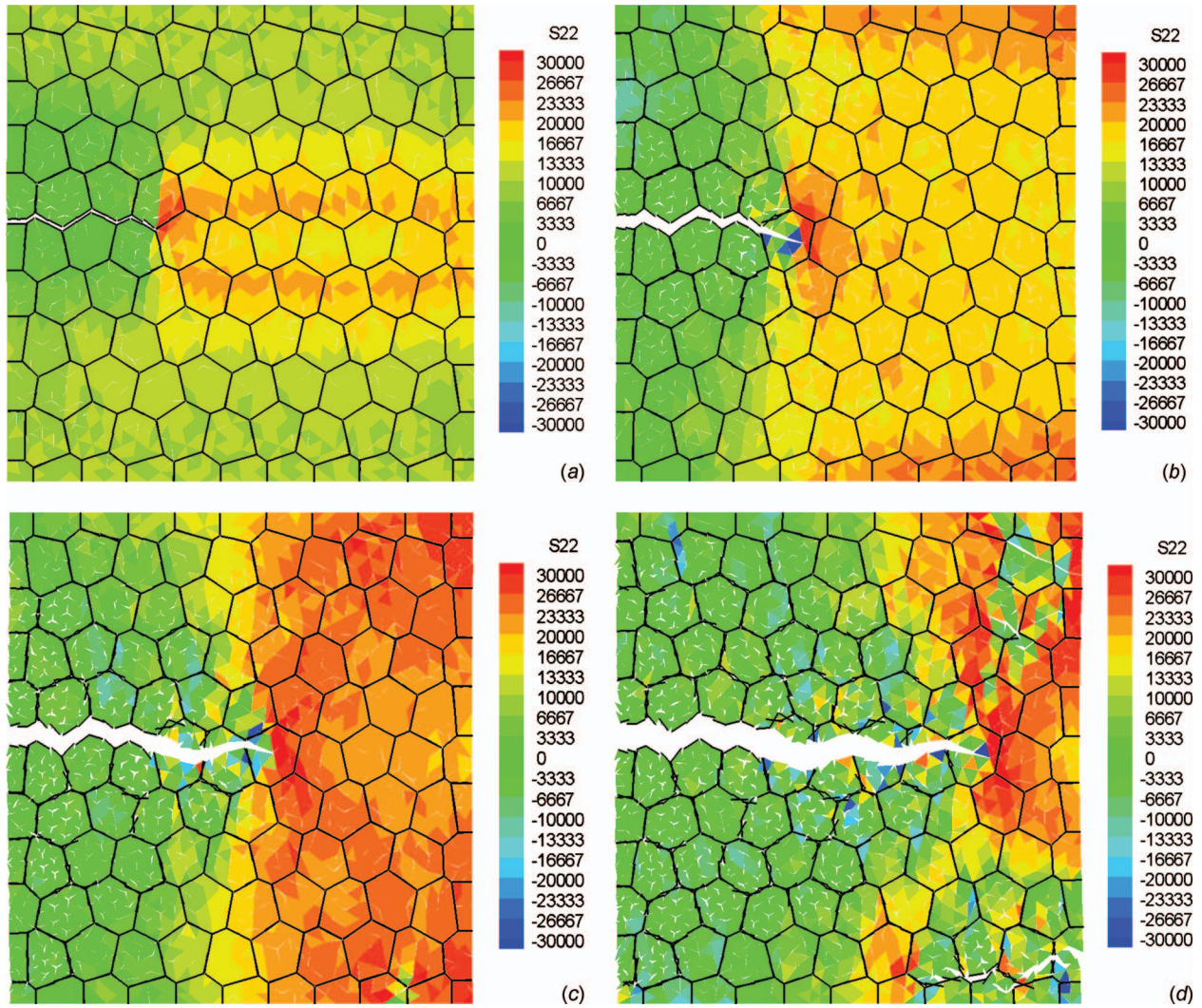
Fig. 6 Intergranular crack propagates through grains: (a) t=1.5 μs, (b) t=2.5 μs, (c) t=3.5 μs, and (d) t=4.5 μs

Consider following linear FEM interpolation in each bulk element:

$$\mathbf{u}^h(\mathbf{X}) = \sum_{I=1}^{n_{node}} N_I(\mathbf{X})\mathbf{d}_I$$

Following the standard FE discretization procedure, e.g., Ref. [25], we have the following discrete equations of motion:

$$\mathbf{M}\ddot{\mathbf{d}} + \mathbf{f}^{int}(\mathbf{d}) - \mathbf{f}^{cohe}(\mathbf{d}) = \mathbf{f}^{ext} \qquad (16)$$

where

$$\mathbf{M} = \underset{e=1}{\overset{n_{elem}}{A}} \int_{B_0^e} \rho_0 \mathbf{N}^{eT}\mathbf{N}^e dV$$

$$\mathbf{f}^{int} = \underset{e=1}{\overset{n_{elem}}{A}} \int_{B_0^e} \mathbf{B}^{eT}\mathbf{P}^e(\mathbf{d}) dV$$

$$\mathbf{f}^{cohe} = \underset{e=1}{\overset{n_{elem}}{A}} \int_{S_c^e} \mathbf{N}^{eT}\mathbf{T}_e^{cohe} dS$$

$$\mathbf{f}^{ext} = \underset{e=1}{\overset{n_{elem}}{A}} \left\{ \int_{B_0^e} \mathbf{N}^{eT}\mathbf{B}^e dV + \int_{\partial_t B_0^e} \mathbf{N}^{eT}\bar{\mathbf{T}}^e dS \right\}$$

where A is the element assemble operator, $\mathbf{N}^e$ is the element shape function matrix, and $\mathbf{B}^e$ is the element B-matrix.

The explicit time integration based Newmark-β method with $\beta=0$ [26] is used in displacement update

$$\mathbf{d}_{n+1} = \mathbf{d}_n + \mathbf{v}_n \Delta t_n + \frac{1}{2}\mathbf{a}_n(\Delta t_n)^2$$

$$\mathbf{a}_{n+1} = \mathbf{M}^{-1}(\mathbf{f}^{ext} - \mathbf{f}^{int} + \mathbf{f}^{cohe})$$

$$\mathbf{v}_{n+1} = \mathbf{v}_n + \frac{1}{2}(\mathbf{a}_n + \mathbf{a}_{n+1})\Delta t_n \qquad (17)$$

where $\mathbf{d}_n$ is the displacement field at the time step at time step n, $\mathbf{v}_n$ is the velocity field at the time step n, and $\mathbf{a}_n$ is the acceleration field at the time step n. The subscripts n and $n+1$ denote to quantities evaluated at times t_n and t_{n+1}. After the displacement field is updated, the deformation gradient in each bulk element can be calculated as

$$\mathbf{F}_n^e = \mathbf{I} + \sum_{I=1}^{n_{node}} \mathbf{B}_I^e \mathbf{d}_n^e \qquad (18)$$

and subsequently, the stress measures can then be updated.

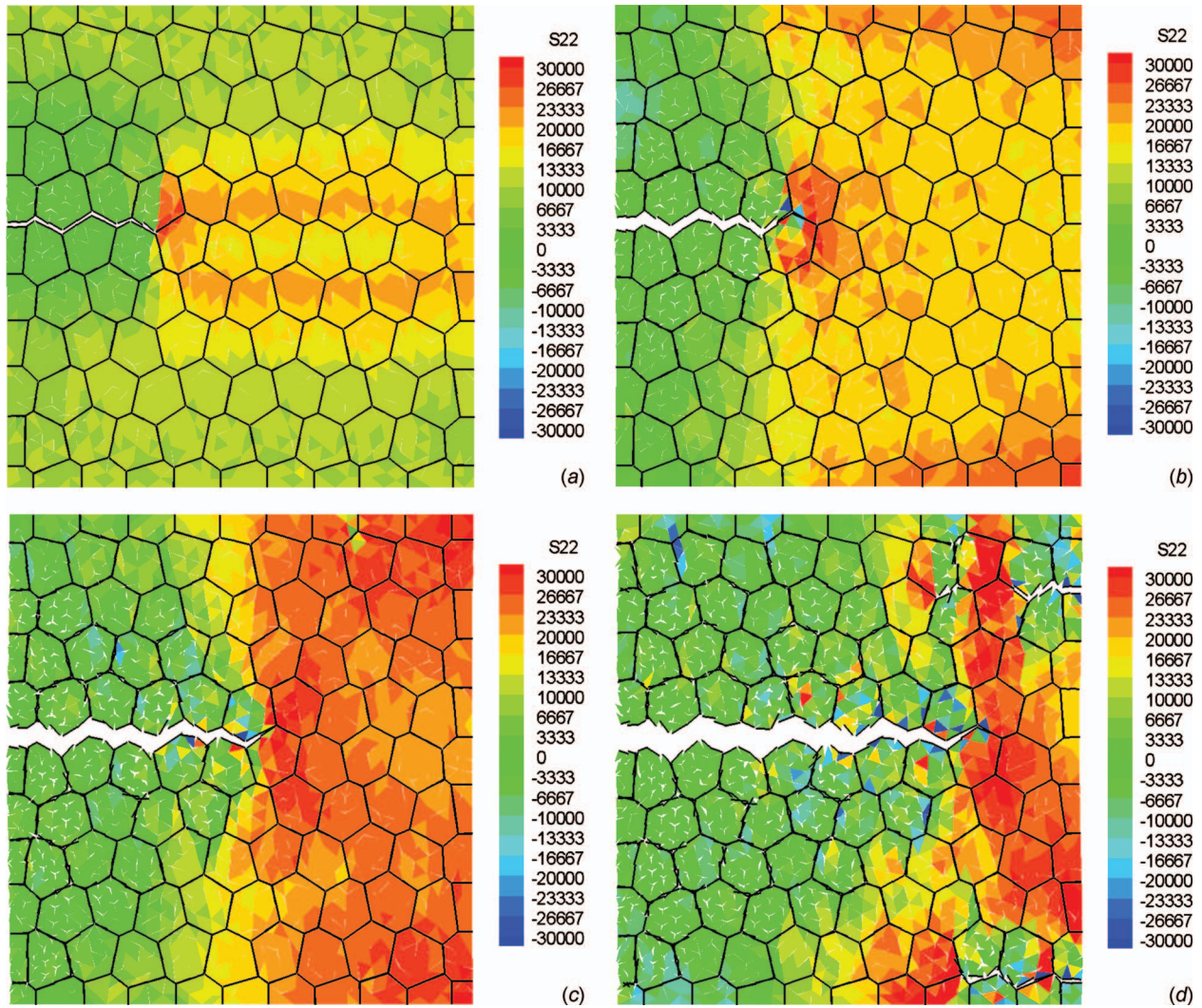**Fig. 7 Transgranular crack propagates along grain boundaries:** (*a*) t=1.5 μs, (*b*) t=2.5 μs, (*c*) t=3.5 μs, and (*d*) t =4.5 μs

Similarly, the effective deformation gradient in each cohesive element can be also updated. For the case of plane strain, it is updated based on the following equations:

$$
\begin{bmatrix} F^c_{11}(t_n) \\ F^c_{12}(t_n) \\ F^c_{21}(t_n) \\ F^c_{22}(t_n) \end{bmatrix} = \begin{bmatrix} 1 \\ 0 \\ 0 \\ 1 \end{bmatrix} + \frac{1}{LR_0} \begin{bmatrix} d & 0 & -b & 0 \\ -c & 0 & a & 0 \\ 0 & d & 0 & -b \\ 0 & -c & 0 & a \end{bmatrix}
$$
$$
\times \begin{bmatrix} u^+_{I+1}(t_n) - u^-_I(t_n) \\ v^+_{I+1}(t_n) - v^-_I(t_n) \\ u^+_I(t_n) - u^-_{I+1}(t_n) \\ v^+_I(t_n) - v^-_{I+1}(t_n) \end{bmatrix} \quad (19)
$$

where $(u^\pm_I(t_n), v^\pm_I(t_n)) = \mathbf{d}^\pm_I(t_n)$ and the meaning of the superscripts $\pm$ are referred to Fig. 2 for their definitions; L is side length of the adjacent bulk elements and R_0 is the thickness of the cohesive element. The constants, a, b, c, d are defined in Eq. (8). The stress inside the cohesive zone can then be updated by using Eq. (12).

5 Numerical Simulations

5.1 Fracture in Polycrystalline Material. In this example, the test specimen is a 2D plate with a dimension of 2 mm $\times 2$ mm that is subjected to unilateral tension in Y-axis (see Fig. 5(*a*)). As shown in Fig. 5(*b*), there are 121 grains and 2376 bulk elements in this model. Also, a precrack is set along several grain boundaries on the left side of the plate. During the calculation, the time step is chosen as $\Delta t = 1 \times 10^{-10}$ s. For the first case, the depletion potentials in both the cohesive zones in grains and the grain boundary have the same depth, i.e., $\epsilon^g_{\mathrm{depl}} = \epsilon^{gb}_{\mathrm{depl}}$. From Fig. 6, it can be seen that crack propagation can go through grains. However, if the cohesive strength in the cohesive zones inside the grains are set to be much stronger than that of the grain boundary, e.g., $\epsilon^g_{\mathrm{depl}} = 5\epsilon^{gb}_{\mathrm{depl}}$, the crack path will only follow grain boundaries as shown in Fig. 7. In addition, some minor cracks can be watched around the main crack surface and tip for the reason of crack bifurcation. Although the grain shape looks uniform in the current example, there is no technical difference or difficulty to apply this method to polycrystalline solids with grains in random shape.

5.2 Convergence Test. Generally, the results of the cohesive method are sensitive to its elements size. To test the effects of mesh size in a multiscale cohesive zone method, a unilateral tension test is implemented with four different meshes and the test specimen is a 2D plate with a dimension of 0.02 mm $\times 0.02$ mm, which contains 121 grains. Constant velocity boundary condition is applied on both top and bottom edges. Moreover, the ration ρ between the average element size and average grain
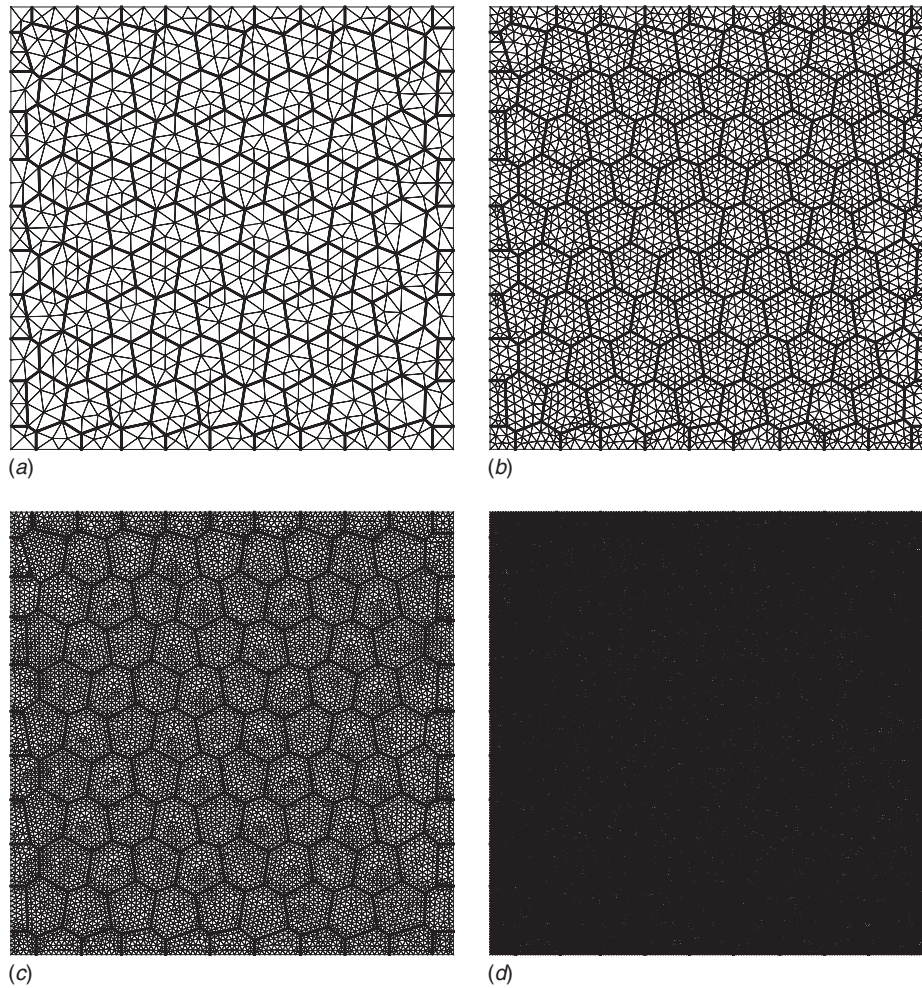
Fig. 8 Different meshes over grains: (*a*) case 1 $\rho=0.5$, (*b*) case 2 $\rho=0.2$, (*c*) case 3 $\rho=0.1$, and (*d*) case 4 $\rho=0.05$

size is chosen to define mesh density. Hereby, four cases, which are corresponding to $\rho=0.5,0.2,0.1,0.05$, are employed as shown in Fig. 8. Meanwhile, cohesive strength in the cohesive zones inside grains is set to be stronger than that of the grain boundary. As a result, Fig. 9 shows the crack propagation in the specimen. It can be seen clearly that the crack propagates along same grain boundaries although mesh density varies so much.

On the other hand, the total reaction forces r_f^i on top edge are calculated in each case for further comparison. As illustrated by Fig. 10, the reaction forces becomes closer as mesh density increases. For a quantitative comparison, the error between two cases is defined as

$$\text{Err}_i = \int_0^t |r_f^i - r_f^{i-1}|dt, \quad i=2,3,4 \tag{20}$$

The errors are listed in Table 1. The error decreases as the element size becomes smaller.

5.3 Simulations of High-Speed Impact and Spall Fracture. To further demonstrate the versatility of the method, numerical simulations have been carried out to simulate high-speed impact induced spall fractures, which is a very difficult problem that has been elusive to many existing numerical methods [27]. The exact problem statement is described in Fig. 11. The projectile is a rigid block with an impact velocity of $v=200$ m/s, the target is a 1 mm $\times$ 2 mm block with free boundary. In this example, there are a total of 861 grains and 4838 triangular bulk elements in the

target. The lattice orientation settings for both the bulk element, as well as the cohesive zone, are exactly the same as in the extension example 5.1.

In time integration, the time step is chosen as $\Delta t = 1 \times 10^{-10}$ s. Contact problems are characterized by impenetrability conditions that needs to be enforced during computation. We adopted the exact enforcement of the impenetrability condition in a single time step [28]. The wave propagation from the contact point to the opposite boundary has been observed. The phenomena of spall fracture under impacts has been captured and are shown in Figs. 12 and 13.

6 Conclusions

In this work, we have applied the multiscale cohesive zone model to simulate dynamic fracture in polycrystalline solids. A major advantage of the multiscale cohesive zone model over the conventional cohesive finite element method is that it can accurately formulate the interface depletion potential to represent the mesoscale material properties of the interface. Utilizing this advantage, we have demonstrated that one can use the multiscale cohesive zone finite element analysis to model the grain boundary with accuracy and flexibility to such extent that has not been achieved before.

First, the multiscale cohesive zone model can predict both intergranular and transgranular fractures and their transitions by adjusting grain boundary lattice orientation and cohesive strength. Second, the method is applied to simulate spall fracture induced
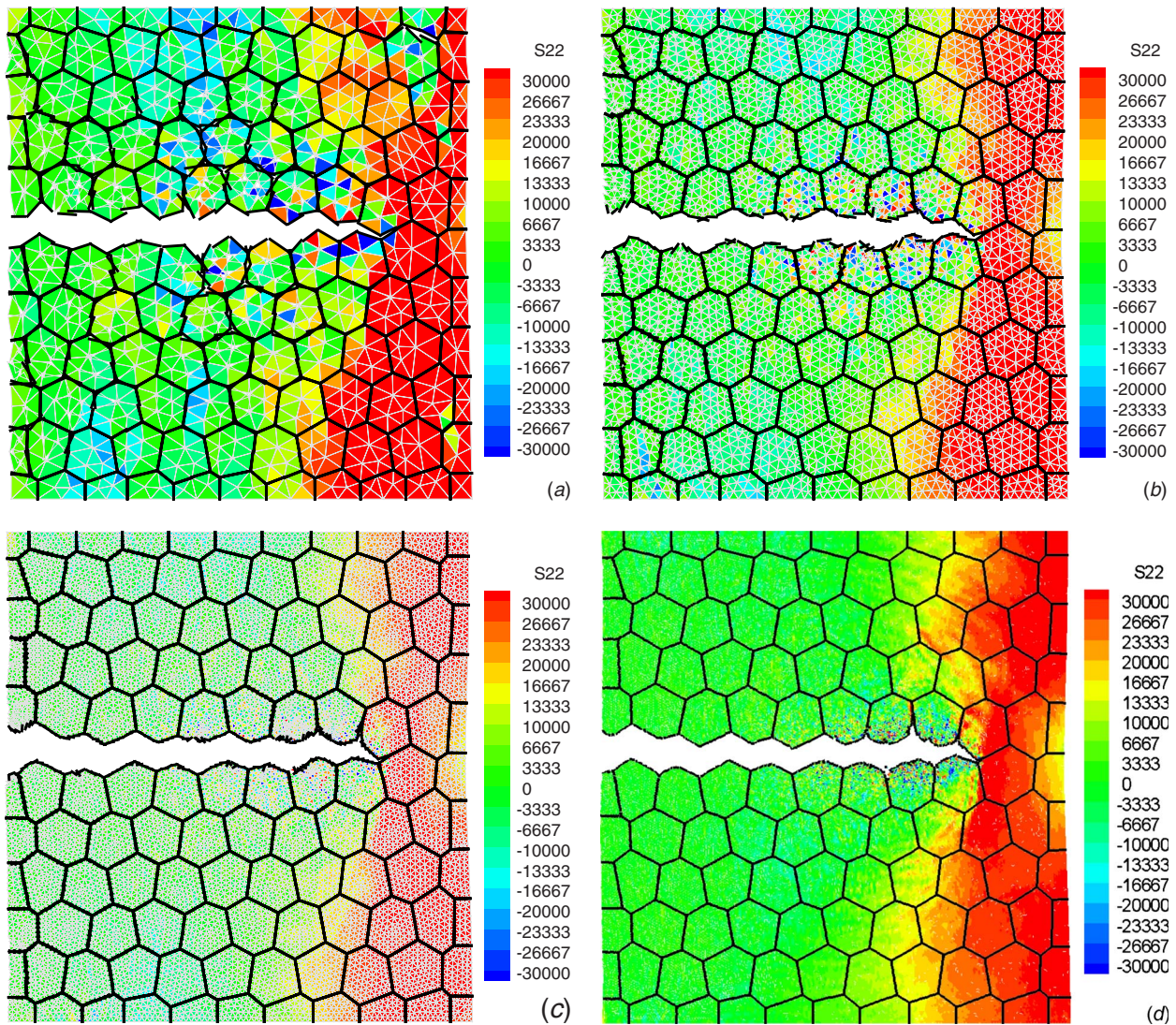
Fig. 9 Crack surfaces calculated by different meshes: (*a*) case 1 ρ=0.5, (*b*) case 2 ρ=0.2, (*c*) case 3 ρ=0.1, and (*d*) case 4 ρ=0.05
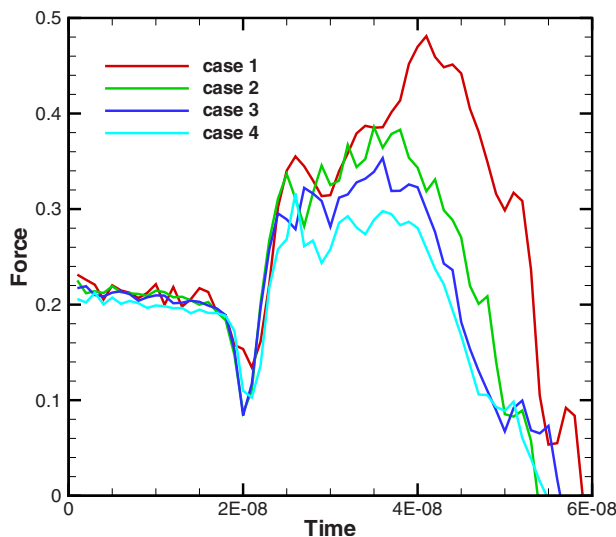

Fig. 10 Reaction force varies along time

by high-speed impact loads without adding any artificial viscosities. The numerical simulations show excellent qualitative agreement with the experimental observation. A further study on the quantitative comparison in surface velocity, as well as in microstructure evolution during the impact, is underway and it will be reported in elsewhere.

We would like to stress that a main difference between the multiscale cohesive zone model and the conventional cohesive finite element method is how to construct interfacial surface cohesive potential. In the conventional cohesive finite element method, the empirical cohesive traction-separation relation is imposed and the prescribed cohesive traction-separation relation is fixed in the sense that it does not take into account some important

Table 1 Comparison of different meshes

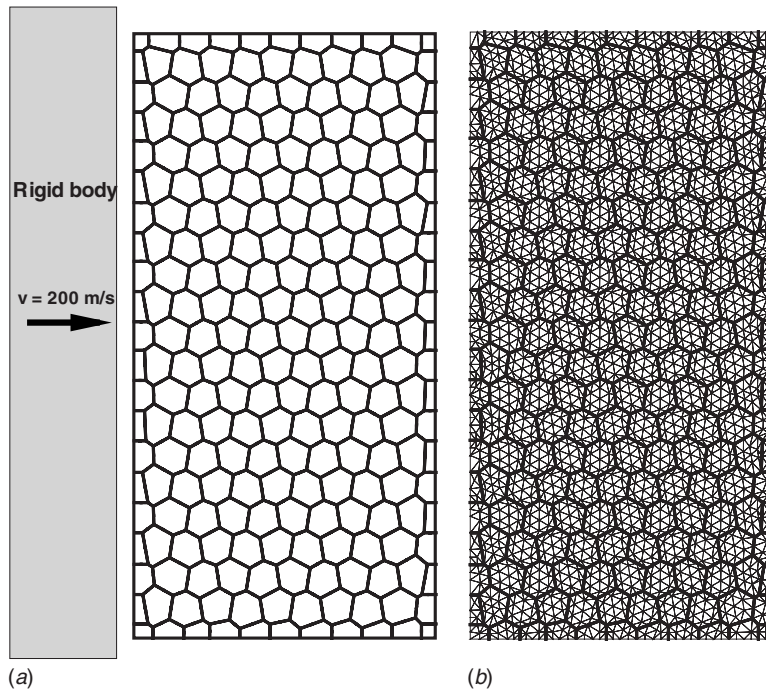| ρ	Element size (μm)	Bulk elements	Error
0.5	1	1428	
0.2	0.5	6041	3.869×10^{-09}
0.1	0.2	18,612	1.652×10^{-09}
0.05	0.1	67,182	1.627×10^{-09}

Fig. 11 Examples of high-speed impact: (*a*) sketch of impact model and (*b*) mesh of the plate
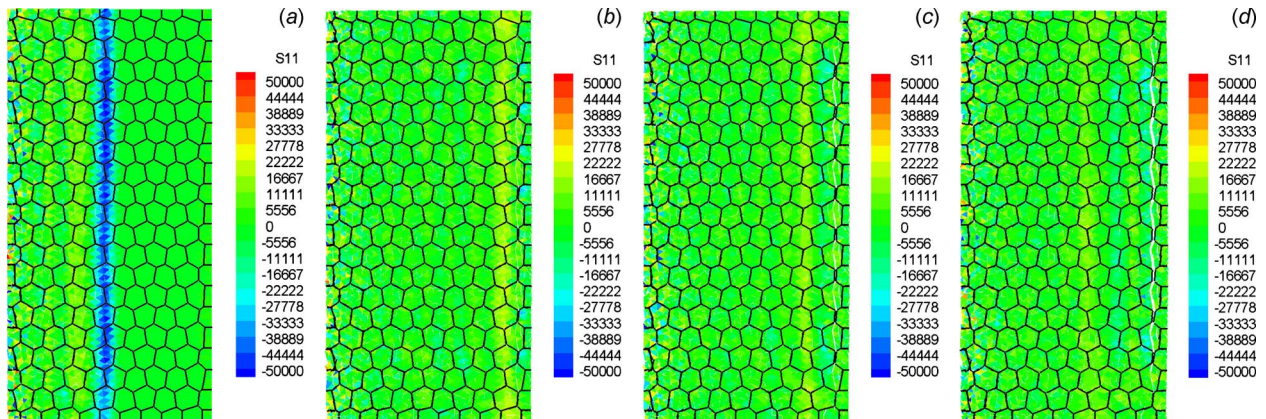
Fig. 12 Intergranular spall fracture propagates through grains: (*a*) t=1.0 μs, (*b*) t=1.2 μs, (*c*) t=1.3 μs, and (*d*) t =1.5 μs

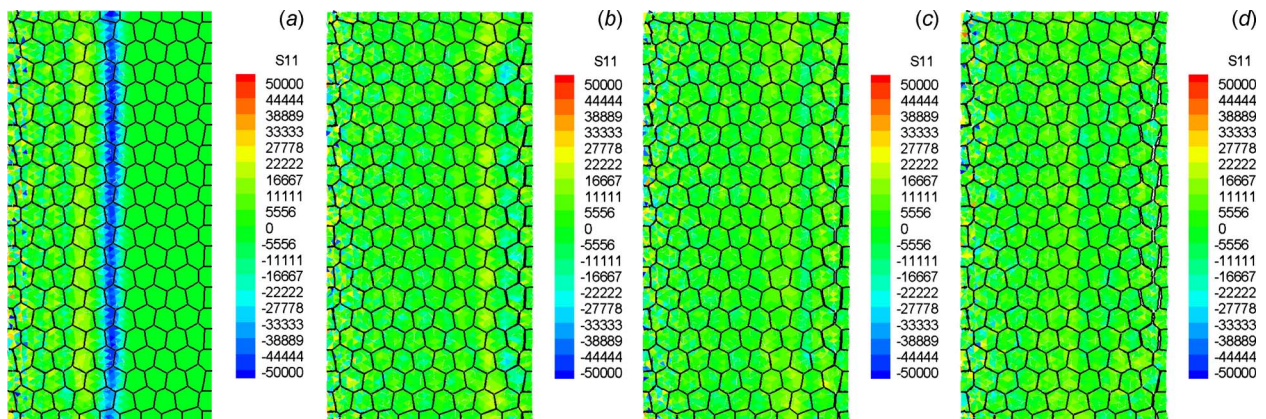**Fig. 13 Transgranular spall fracture propagates along grain boundaries:** (*a*) t=1.0 μs, (*b*) t=1.2 μs, (*c*) t=1.3 μs, and (*d*) t=1.5 μs

physical characteristics of interfacial fracture, such as interface orientation, its orientation difference with adjacent bulk elements, and interface microstructures. In fact, in the conventional cohesive finite element, one always uses one set of interface cohesive laws to model every cohesive zone. It implicitly views the interface cohesive laws being as a universal constitutive relation as the bulk constitutive relations that are frame-indifferent and objective. Therefore, in conventional cohesive finite element method, there is basically no difference between the mixed mode fracture, as well as the mode-specific fracture, because the interface cohesive laws remain the same. That is the primary reason why we have so many difficulties in practice to match its results with experimental results. Whereas in the multiscale cohesive zone model, the only objective constitutive relation is again the bulk constitutive relation and the interface constitutive relation is a derivative of the constitutive relation in the bulk cohesive zone and they change from interface to interface, from stress state (hence loading conditions) to stress state. It is because of this difference that the multiscale cohesive zone method provides a better, flexible, and efficient means to simulate fractures in polycrystalline solids.

Last, to probe mesh-dependence and mesh-sensitivity of the method, we have conducted a numerical convergence study based on the Cauchy sequence limit criterion. The numerical results suggest that the method is robust enough to produce convergent results.

Acknowledgment

References

[1] Bunge, H. J., 1992, *Texture Analysis in Material Science*, Butterworths, London, UK.
[2] Hosford, W. F., 1996, "On the Basis of Yield Criteria," Textures Microstruct., **26**, pp. 479–493.
[3] Kocks, U. F., Tome, C., and Wenk, H. R., 1997, *Texture and Anisotropy. Preferred Orientations in Polycrystals and Their Effect on Material Properties*, Cambridge University Press, Cambridge, UK.
[4] Zhou, Y., Jonas, J. J., Savoie, J., Makinde, A., and MacEwen, S. R., 1998, "Effect of Texture on Earing in FCC Metals: Finite Element Simulations," Int. J. Plast., **14**, pp. 117–138.
[5] Bhattacharyya, A., El-Danaf, E., Kalidindi, S. R., and Doherty, R. D., 2001, "Evolution of Grain-Scale Micro-Structure During Large Strain Simple Compression of Polycrystalline Aluminum With Quasi-Columnar Grains: OIM Measurements and Numerical Simulation," Int. J. Plast., **17**, pp. 861–883.
[6] Espinosa, H. D., and Zavattieri, P. D., 2003, "A Grain Level Model for the Study of Failure Initiation and Evolution in Polycrystalline Brittle Materials. Part I: Theory and Numerical Implementation," Mech. Mater., **35**, pp. 333–364.
[7] Bažant, Z., and Oh, B., 1985, "Microplane Model for Progressive Fracture of Concrete and Rock," J. Eng. Mech., **111**, pp. 559–582.
[8] Addessio, F., and Johnson, J., 1999, "A Constitutive Model for the Dyamic Response of Brittle Materials," Alamos National Laboratory, Report No. LA-UR-89-2651.
[9] Curran, D., Seaman, L., Cooper, T., and Shockey, D., 1990, "Micromechanical Model for Comminution and Granular Flow of Brittle Material Under High Strain Rate Application to Penetration of Ceramic Targets," Int. J. Impact Eng., **13**, 53–83.
[10] Espinosa, H. D., 1995, "On the Dynamic Shear Resistance of Ceramic Composites and Its Dependence on Applied Multiaxial Deformation," Int. J. Solids Struct., **32**, pp. 3105–3128.
[11] Clayton, J. D., 2005, "Modeling Dynamic Plastic and Spall Fracture in High-Density Polycrystalline Alloys," Int. J. Solids Struct., **42**, pp. 4613–4640.
[12] Lawn, B., 1993, *Fracture of Brittle Solid*, Cambridge University Press, Cambridge, UK.
[13] Xu, X.-P., and Needleman, A., 1994, "Numerical Simulations of Fast Crack Growth in Brittle Solids," J. Mech. Phys. Solids, **42**, pp. 1397–1434.
[14] Ortiz, M., and Pandolfi, A., 1999, "Finite-Deformation Irreversible Cohesive Elements for Three-Dimensional Crack-Propagation Analysis," Int. J. Numer. Methods Eng., **44**, pp. 1267–1282.
[15] Wells, G. N., and Sluys, L. J., 2001, "A New Method for Modelling Cohesive Crack Using Finite Elements," Int. J. Numer. Methods Eng., **50**, pp. 2667–2682.
[16] Moës, N., and Belytschko, T., 2002, "Extended Finite Element Method for Cohesive Crack Growth," Eng. Fract. Mech., **69**, pp. 813–833.
[17] Liu, X., Li, S., and Sheng, N., 2008, "A Cohesive Finite Element for Quasi-Continua," Comput. Mech., **42**, pp. 543–553.
[18] Zeng, X. W., and Li, S., 2010, "A Multiscale Cohesive Zone Model and Simulations of Fracture," Comput. Methods Appl. Mech. Eng., **199**, pp. 547–556.
[19] Israelachvili, J., 1991, *Intermolecular and Surface Forces*, Academic, New York.
[20] Hill, R., 1972, "On Constitutive Macro-Variables for Heterogeneous Solids at Finite Strain," Proc. R. Soc. London, Ser. A, **326**, pp. 131–147.
[21] Ghosh, S., and Yunshan, L., 1995, "Voronoi Cell Finite Element Model Based on Micropolar Theory of Thermoelasticity for Heterogeneous Materials," Int. J. Numer. Methods Eng., **38**, pp. 1361–1398.
[22] Bolander, J., and Saito, S., 1998, "Fracture Analyses Using Spring Networks With Random Geometry," Eng. Fract. Mech., **61**, pp. 569–591.
[23] Liu, Y., Kageyama, Y., and Murakami, S., 1998, "Creep Fracture Modeling by Use of Continuum Damage Variable Based on Voronoi Simulation of Grain Boundary Cavity," Int. J. Mech. Sci., **40**, pp. 147–158.
[24] Espinosa, H. D., and Zavattieri, P. D., 2003, "A Grain Level Model for the Study of Failure Initiation and Evolution in Polycrystalline Brittle Materials. Part II: Numerical Examples," Mech. Mater., **35**, pp. 365–394.
[25] Hughes, T. J. R., 1987, *The Finite Element Method: Linear Static and Dynamic Finite Element Analysis*, Prentice-Hall.
[26] Belytschko, T., 1983, "An Overview of Semidiscretization and Time Integration Procedure," *Computational Methods for Transient Analysis*, T. Belytschko and T. J. R. Hughes, eds., North-Holland, Amsterdam, pp. 1–65.
[27] Antoun, T., Seaman, L., Curran, D. R., and Kanel, G. I., 2003, *Spall Fracture (Shock Wave and High Pressure Phenomena)*, Springer, New York.
[28] Hughes, T. J. R., Talor, R., Sackman, J., Curnier, A., and Kamoknukulchai, W., 1976, "A Finite Element Method for a Class of Contact-Impact Problem," Comput. Methods Appl. Mech. Eng., **8**, pp. 249–276.